Quantification of carbonated Mg-based cement pastes by Raman spectroscopy

Mi, Tangwei; Chen, Xi; Yang, En-Hua; Unluer, Cise

Published in:
Cement and Concrete Research

DOI:
10.1016/j.cemconres.2024.107454

Publication date:
2024

Cement and Concrete Research 178 (2024) 107454

Contents lists available at ScienceDirect

Cement and Concrete Research

journal homepage: www.elsevier.com/locate/cemconres

Quantification of carbonated Mg-based cement pastes by Raman spectroscopy

Tangwei Mi [a], Xi Chen [a], En-Hua Yang [a], Cise Unluer [b,*]

[a] School of Civil and Environmental Engineering, Nanyang Technological University, 50 Nanyang Avenue, 639798, Singapore
[b] Department of Mechanical, Aerospace and Civil Engineering, University of Manchester, Manchester M13 9PL, United Kingdom

ARTICLE INFO

Keywords:
MgO (D)
Carbonation (C)
Characterization (B)
Spectroscopy (B)
X-ray diffraction (B)

ABSTRACT

This study presented a detailed investigation of the carbonation of reactive magnesia cement (RMC) and brucite cement by using Raman spectroscopy and other characterization techniques. Quantification of carbonation at different depths and formation of various reaction products in each system were demonstrated. Correlations between Raman peak intensities and carbonation degree were established by Raman mapping. Established correlations were employed to evaluate the carbonation behaviour of RMC and brucite cement. Results indicated the higher sensitivity of Raman spectroscopy than XRD in detecting different carbonation products at early stages. This information can be used to assess the strength and microstructural development of RMC and brucite cement since different HMCs have distinct properties and performance contributions, and their transformation plays a key role in microstructural and strength development. This study provided further understanding of the carbonation mechanisms of Mg-based systems, which could enable carbonation degree and performance prediction via the established correlations.

1. Introduction

Production of ordinary Portland cement (OPC) accounts for around 5–7 % of the global carbon dioxide (CO_2) emissions [1,2], which is mainly associated with the decomposition of limestone and burning of fuels for calcination [3]. To address this issue, a range of alternative cementitious materials with potentially lower CO_2 emissions are being investigated. One of these is Mg-based cements produced from desalination reject brine, whose potential and technical feasibility as an alternative cementitious material has been reported in previous studies [4–7]. Reactive MgO cement (RMC) that can be obtained at the end of this process can gain strength by reacting with CO_2 and forming hydrated magnesium carbonates (HMCs) [4,8,9] such as needle-like nesquehonite ($MgCO_3{\cdot}3H_2O$), disk/rosette-like hydromagnesite ($4MgCO_3{\cdot}Mg(OH)_2{\cdot}4H_2O$), dypingite ($4MgCO_3{\cdot}Mg(OH)_2{\cdot}5H_2O$) and artinite [10,11]. Considering the importance of carbonation for the strength development of RMC-based systems, it is critical to understand their carbonation behaviour in terms of the composition of reaction products and overall carbonation degree [12,13].

Various carbonation products have been reported for Mg-based systems in the literature, as summarised in Fig. 1. Generally, the formation of different types of HMCs is highly dependent on the curing conditions (i.e. temperature and CO_2 concentration) and precursor (i.e. RMC or brucite). The most common carbonation product for RMC-based mixes is nesquehonite at temperatures below 100 °C. When the temperature is increased to up to 400 °C, nesquehonite transfers to hydromagnesite/artinite. Whilst this trend is generally recognised, there is a disagreement on the compositions of carbonation products forming at room temperature (i.e. 25–30 °C) and the transformation of HMCs under different conditions [14–17]. Under a CO_2 concentration of 20 % (80 ± 5 % humidity and 30 ± 1.5 °C), dypingite, hydromagnesite, nesquehonite and artinite were all reported as the carbonation products of RMC by [18], whilst artinite was not mentioned by [19], and dypingite was absent in Dung, Hay, Lesimple, Celik and Unluer [9,20]. These disagreements could be explained by variations in mix design and carbonation duration. Similar differences in the composition of carbonated RMC matrices could also be observed under a CO_2 concentration of 10 % at room temperature [5,9,21]. These differences might have been caused by other factors, such as variations in curing times and pressures. When brucite was used as the precursor instead of RMC, further variations in the carbonation products were observed. Instead of nesquehonite, hydromagnesite was reported as the most common

* Corresponding author.
E-mail address: cise.unluer@manchester.ac.uk (C. Unluer).

https://doi.org/10.1016/j.cemconres.2024.107454
Received 24 September 2023; Received in revised form 22 January 2024; Accepted 30 January 2024
Available online 3 February 2024

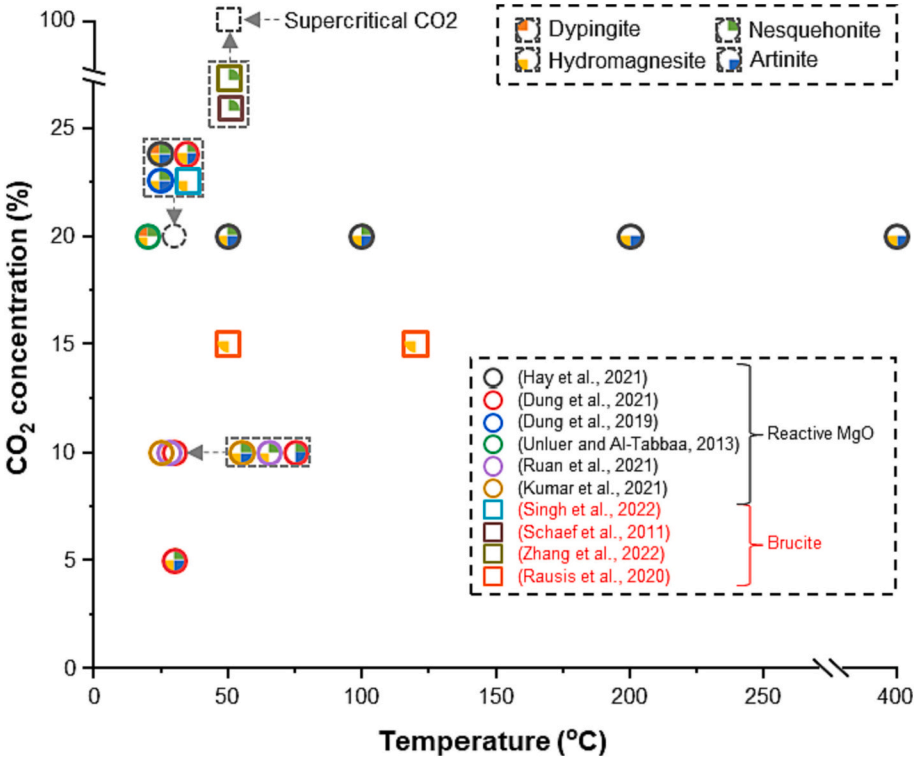

Fig. 1. Carbonation products observed within Mg-based systems under different CO_2 concentrations and temperatures [4,5,9,18–24].

product observed when the CO_2 concentration was below 20 % [4,22]. Nesquehonite was only detected when brucite was exposed to supercritical CO_2 [23,24]. These variations in the findings of the carbonation products in RMC- and brucite-based cements can create undesirable uncertainties during their practical application.

In addition to their composition, the amount of reaction products after carbonation also plays a significant role in the strength development of RMC- and brucite-based cements. Current techniques to quantify the carbonation products include spraying with phenolphthalein [25,26], acid digestion [27], thermogravimetric analysis (TGA) [28] and X-ray diffraction (XRD) [29], which have provided valuable information towards understanding the carbonation behaviour of these binder systems [9,18,29–31]. However, each of these techniques present certain shortcomings. For instance, use of phenolphthalein can underestimate carbonation depth since it can only identify pH over/below 9, whilst the partially carbonated areas may be overlooked [32,33]. Alternatively, acid digestion was found to overestimate the carbonated content due to the high volatility of the acid, and the heat emitted from the reaction between carbonates and acid [19]. Moreover, though TGA can capture the precise mass loss of carbonated products, their chemical compositions can be hardly differentiated [34]. Additionally, besides the phenolphthalein spray, all these aforementioned techniques are for bulk analysis (i.e. involving the assessment of a significant quantity of materials in powdered form, commonly a destructive procedure). Therefore, they all fail to continuously monitor the distribution and amount of HMCs at different depths, which strongly affects the strength development of Mg-based systems.

Raman spectroscopy, a backscattering and non-destructive technique, presents certain advantages in characterising and quantifying the carbonation of cementitious systems [35,36]. First, Raman spectroscopy is capable to differentiate various HMCs based on their corresponding characteristic peaks [9,18,37]. Second, there are almost no requirements for special sample preparation and testing conditions (e.g. vacuum) for Raman measurements [38], enabling in-situ measurements without affecting the carbonation processes. Benefiting from these advantages, Raman spectroscopy has been increasingly used in providing relevant information on the carbonation of Mg-based systems [9,18,37]. Moreover, Raman spectroscopy has also been extensively employed in the literature to quantify the carbonation of OPC, resulting in invaluable information regarding the carbonation front and distribution with a high spatial resolution [39–44]. However, for Mg-based systems, Raman spectroscopy has only been employed to identify the phases observed after the carbonation of certain RMC formulations until now. Alternatively, the detailed characterization by Raman spectroscopy and relevant understanding of the formation carbonation products within a range of Mg-based cements including those involving brucite is missing in the literature. More importantly, a critical information gap in the quantification of carbonation products within Mg-based systems by Raman spectroscopy exists due to the absence of correlations between the overall carbonation degree and Raman peak intensities.

Building upon the existing knowledge and methodology developed to quantify the carbonation of OPC [36], this study aims to address these gaps in the literature and provide a detailed understanding of the carbonation products within Mg-based systems via their identification and quantification by Raman spectroscopy. To achieve this, carbonated RMC- and brucite-based cement samples were prepared, which were then mixed with uncarbonated counterparts to simulate varying degrees of carbonation. These samples were then characterized by Raman spectroscopy to establish correlations between the Raman peak intensities and overall carbonation degree. Finally, the established correlations were successfully used to evaluate the carbonation degree of various Mg-based systems subjected to different carbonation curing conditions. The outcome of this work revealed the differences between the carbonation of RMC- and brucite-based cements. More importantly, the feasibility of using the established correlations in the evaluation of the carbonation degree of these systems by Raman spectroscopy was demonstrated.

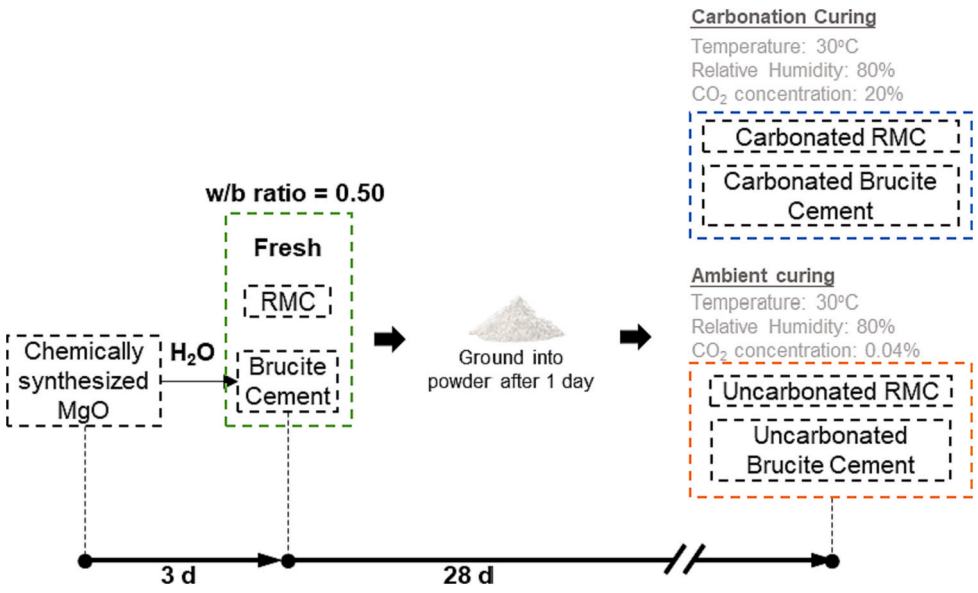

Fig. 2. Schematic representations of sample preparation.

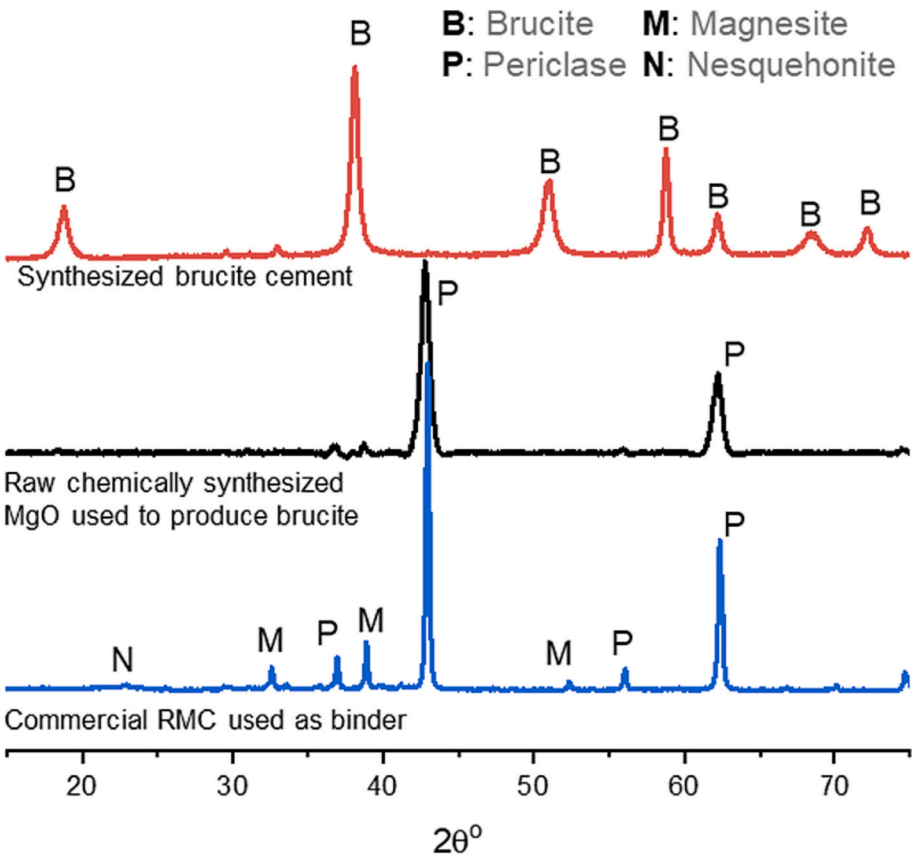

Fig. 3. XRD patterns of commercial RMC, raw chemical MgO (used for brucite production) and produced brucite cement.

2. Materials and methodology

2.1. Materials

Two types of cement, i.e. RMC- and brucite-based, were employed in the present work. The RMC used in the present work was obtained by the calcination of magnesite under 1000 °C from Lingshou Minerals Processing Plant in China with a specific surface area (SSA) of 5.8 m^2/g. The brucite cement was produced via the hydration of a chemically synthesized MgO with a very high reactivity with a SSA of 86.9 m^2/g, obtained from Shanghai Yuanjiang Chemicals Co. Ltd. in China. Deionised water was used for sample preparation.

2.2. Sample preparation

The sample preparation procedure followed in this study is

Table 1
Mix proportions of samples prepared in this study.

	Carbonated RMC (%)	Uncarbonated RMC (%)	Carbonated brucite cement (%)	Uncarbonated brucite cement (%)
R-C0	0	100	–	–
R-C20	20	80	–	–
R-C40	40	60	–	–
R-C60	60	40	–	–
R-C80	80	20	–	–
R-C100	100	0	–	–
B-C0	–	–	0	100
B-C20	–	–	20	80
B-C40	–	–	40	60
B-C60	–	–	60	40
B-C80	–	–	80	20
B-C100	–	–	100	0

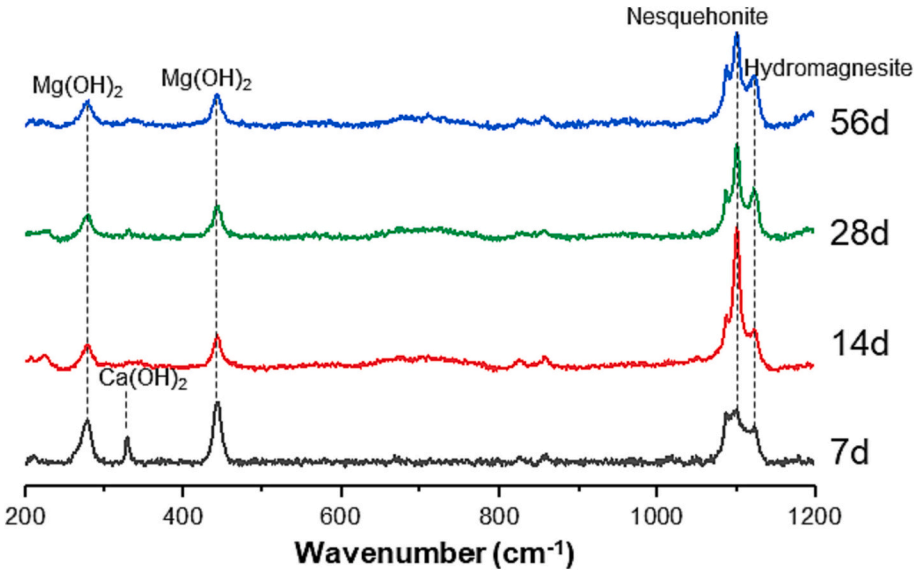

Fig. 4. Raman spectra of carbonated RMC after 7 d, 14 d, 28 d and 56 d of carbonation.

illustrated in Fig. 2. Brucite cement was produced via the hydration of MgO, which was mixed with water at a ratio of 1:10 in a bottle on a rotation machine to promote the hydration process. After 3 days, the precipitated brucite was dried at 50 °C for 3 days in an incubator and ground into powder form (<125 μm). XRD patterns (Fig. 3) were obtained for the commercial RMC, raw chemically synthesized MgO and the produced brucite cement, indicating the total conversion of MgO to brucite. The XRD pattern of RMC presented in Fig. 3 highlighted impurities of magnesites and nesquehonite. RMC- and brucite-based cements were used to prepare pastes with w/b ratio of 0.5. Both pastes were divided into two batches and were ground into powder form (<425 μm) after 1 d to improve their carbonation under two different conditions: (i) accelerated carbonation (30 °C, 80 % relative humidity (RH), and 20 % CO_2 concentration) and (ii) ambient conditions (30 °C, 80 % RH and 0.04 % CO_2 concentration).

After 28 d of accelerated carbonation and ambient curing, four groups of samples were obtained, as shown in Fig. 2. These included carbonated and uncarbonated RMC, and carbonated and uncarbonated brucite cement. It should be noted that the term "carbonated" used here does not imply the complete conversion of all RMC/brucite into HMCs, but that the extent of carbonation reached its limits under the provided conditions, as also demonstrated in earlier studies [4,12,20]. These samples were then mixed at different ratios, as detailed in Table 1. The content of the carbonated phases (%, by mass) was used in labelling each sample. For example, sample R-40 contained 40 % carbonated and 60 % uncarbonated RMC.

Cube samples (20 mm) were also prepared to test the viability of the established correlations in quantifying the carbonation degree of RMC- and brucite-based cements under carbonation curing. Both binders were cast into cubes with a w/b ratio of 0.5, which were then subjected to accelerated carbonation conditions (30 °C, 80 % RH and 20 % CO_2 concentration) for 3 d and 7 d. The cubes were cut in half, and Raman mapping measurements were performed on their cross-sections to evaluate the distribution of carbonation products and overall carbonation degree. To address the potential influence of hydration and natural carbonation during the time interval between sample cutting after carbonation and the Raman scan, the samples were immersed in acetone upon cutting, followed by sealing under vacuum conditions.

2.3. Analysis

2.3.1. Raman spectroscopy

Raman Spectroscopy was performed by using a Renishaw inVia Raman spectrometer equipped with a 738 nm laser and a charge-coupled device (CCD) detector. The laser with a power of ~6 mW was focused via a Newport M-5X (N.A. = 0.10) microscope objective lens into a spot size of ~4 μm in diameter. Raman spectra of the RMC and brucite cement under carbonation curing were obtained at 7 d, 14 d, 28 d and 56 d to identify the characteristic peaks of different carbonated phases and ensure that no further carbonation occurred after 28 days. Each spectrum was recorded with an exposure time of 10 s and two accumulations. Raman mapping measurements were also performed for the samples listed in Table 1. Three random regions were selected on each reference sample with 45 spectra collected from each region,

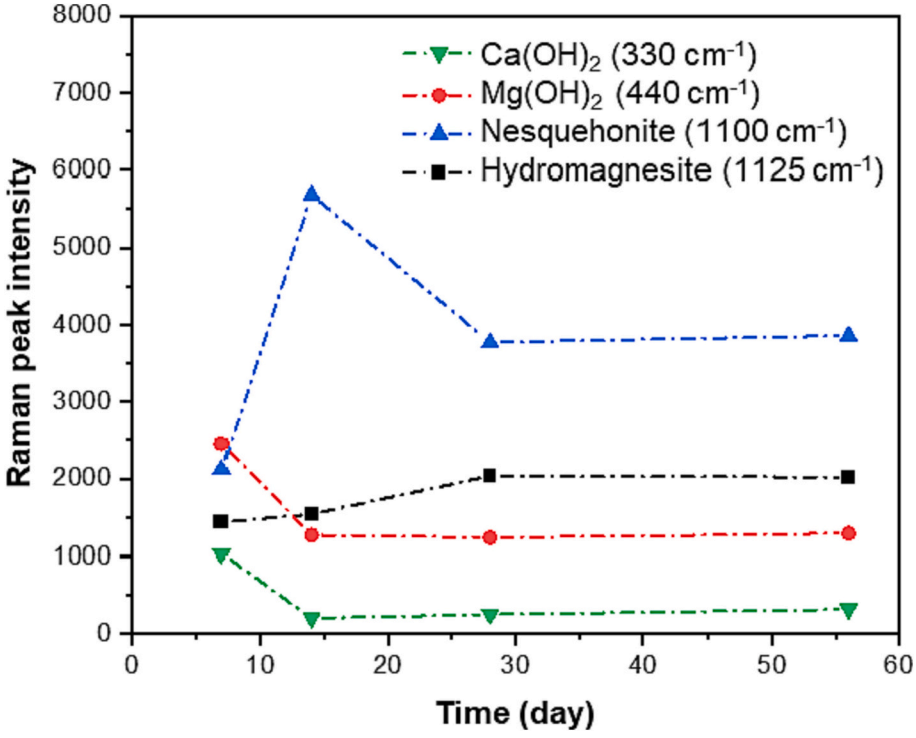

Fig. 5. Evolution of the Raman peaks intensities of carbonated RMC at 330, 440, 1100, and 1125 cm^{-1} with time.

forming a matrix of 5 × 9 in a range of 400 × 800 μm. Raman mappings were also obtained from the cross-section of the cube samples to investigate the carbonation degree. Raman spectra were collected in a matrix of 7 × 31 within a range of 3000 μm in depth from the exposure surface and 600 μm in width at the middle of the cross-section. 7 test points at the same depth were measured to ensure the obtained results were representative of each sample. Each spectrum for Raman mappings was recorded with an exposure time of 5 s and two accumulation times. The obtained spectra were all processed with multiple peak fitting to mitigate the influence of the intensity of one mineral on the other. A demonstration of the multiple peak fitting for the spectra obtained from carbonated RMC and brucite cement is shown in Fig. S1. To eliminate the influence of sample preparation, the sample surfaces were thoroughly polished until uniform surface conditions were achieved.

2.3.2. X-ray diffraction (XRD)

To monitor the transformation of phases and demonstrate that RMC and brucite cement were carbonated after 28 d of accelerated carbonation curing, XRD was performed with a Bruker D8 Advance at 7 d, 14 d, 28 d and 56 d. XRD patterns were obtained via Cu Kα radiation (40 kV, 40 mA) at a scanning rate of 0.5°/step, over a range of 10°–70° (2θ). The effect of preferred orientation on intensity comparison was considered to be negligible due to the consistency in the approach followed during sample preparation and employment of acetone immersion.

2.3.3. Scanning electron microscopy (SEM)

To characterise the microstructure of carbonated RMC and brucite cement, SEM images was obtained by a Zeiss Evo 50 instrument. Samples were vacuum dried before analysis and mounted onto the sample stage by using double-sided adhesive carbon tape. Each sample was coated with gold under 10 mA for 30 s to reduce the charging phenomenon. All SEM images were recorded with an accelerating voltage of 15 kV and a working distance 5–10 mm.

3. Results

3.1. Preparation of carbonated RMC and brucite cement

3.1.1. Raman spectroscopy results

Fig. 4 shows the spectra of carbonated RMC after 7 d, 14 d, 28 d and 56 d of curing. The Raman peak at around 330 cm^{-1} was only observed at 7 d, which corresponded to the presence of $Ca(OH)_2$ [45] as an impurity in RMC. Notably, $Ca(OH)_2$ was not identified using XRD, which should be attributed to the enhanced sensitivity of Raman spectroscopy for its detection [46]. The disappearance of this peak at 14 d, 28 d and 56 d should be attributed to the carbonation of $Ca(OH)_2$. Generally, 5 Raman peaks at 279, 440, 1087, 1100 and 1125 cm^{-1} were observed in all spectra, among which 280 and 440 cm^{-1} were assigned to the O—H vibration modes of brucite [20,47]. Although the peak at 1087 cm^{-1} was unassigned after a comprehensive evaluation of existing literature and experimental findings, the intensity variation at 1087 cm^{-1} correlated closely with changes observed at 280 and 440 cm^{-1}. Furthermore, the Raman spectrum of brucite in the RRUFF database (Brucite R040077) exhibited a peak at a similar position, as shown in Fig. S2, suggesting the peak at 1087 cm^{-1} could be related to the presence of $Mg(OH)_2$, whilst no relevant vibration mode near the Raman shift of 1087 cm^{-1} was reported. The peak at ~1100 cm^{-1} corresponded to the symmetric stretching of the CO_3^{2+} ion in nesquehonite [48,49], whilst the peak at ~1125 cm^{-1} was related to the symmetric stretching mode of the C—O bond in hydromagnesite [49]. The intensity of these peaks changed with carbonation duration, which was associated with the conversion of brucite into HMCs.

To compare the evolution of chemical compositions with carbonation duration, the intensities of the most intense peaks of each compound, i.e., 330, 440, 1100, and 1125 cm^{-1}, are depicted in Fig. 5. The amounts of $Ca(OH)_2$ and $Mg(OH)_2$ both demonstrated decreasing trends from 7 d to 28 d, revealing their continuous carbonation. Conversely, the amount of hydromagnesite, one of the major HMCs, increased during the same period (7 d to 28 d). However, the amount of nesquehonite increased from 7 d to 14 d and decreased from 14 d to 28 d. This could be

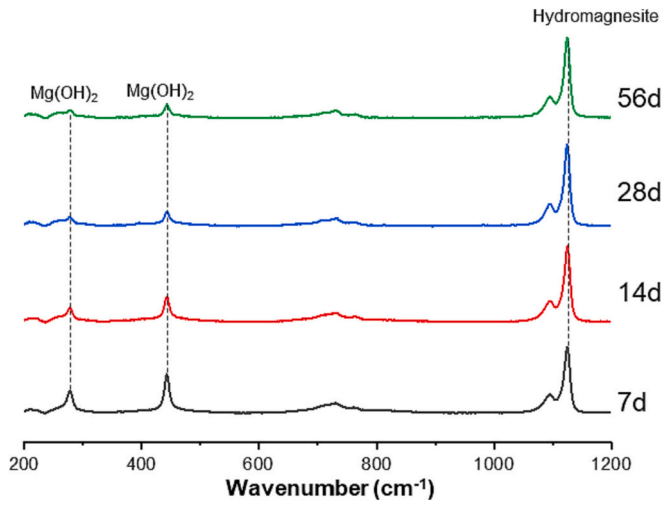

Fig. 6. Raman spectra of carbonated brucite cement after 7 d, 14 d, 28 d and 56 d of carbonation.

caused by the transformation of nesquehonite to hydromagnesite, which was consistent with the findings presented in the literature [17,50–52]. There were no significant changes in the peak intensities between 28 d and 56 d, indicating that the RMC-based binder reached a maximum carbonation degree at 28 d under the conditions provided. In this context, "carbonation degree" was defined under the specific conditions of the current investigation. It is distinct from "carbonation content (%)", as the matrix achieving the maximum carbonation degree did not undergo full conversion, therefore achieving <100 %. Overall, the carbonation of RMC mainly induced the formation of nesquehonite and hydromagnesite, with a saturation of carbonation at around 28 d.

The Raman spectra obtained from carbonated brucite cement are shown in Fig. 6. Three sharp Raman peaks could be observed in all spectra, including 279, 440 and 1125 cm^{-1}. The first two peaks were related to the O—H vibration modes of brucite [20,47], whilst the last peak was associated with the C—O vibration mode of CO_3^{2+} in hydromagnesite [49]. The carbonation product of brucite cement was mainly hydromagnesite, whilst nesquehonite was absent.

To reveal the evolution of chemical compositions of carbonated brucite cement, Fig. 7 shows the changes in the intensities of the characteristic Raman peaks of brucite and hydromagnesite at 440 and 1125 cm^{-1}, respectively. Overall, brucite demonstrated a constant decreasing trend up to 28 d, whilst hydromagnesite showed a completely inverse trend, linked with the carbonation of brucite to form hydromagnesite. Similar to RMC, the carbonation of brucite reached a maximum degree at 28 d since with no significant changes in the amounts of brucite and hydromagnesite observed at 56 d. In summary, further carbonation of brucite could barely occur after 28 d, whereas the main carbonation product was hydromagnesite.

3.1.2. *X-ray diffraction (XRD) results*

Fig. 8 shows the XRD patterns of carbonated RMC at different ages of carbonation. Presence of unreacted MgO, shown as periclase, even after 56 d of carbonation was observed, with the most intense peaks located at 42.9° and 62.3° (2θ) [53]. Considering the intensities of these peaks, periclase remained the predominant compound in the carbonated RMC. The peaks at 18.1°, 38.0°, 50.8° and 58.6° (2θ) were assigned to the brucite [54,55]. The major HMC identified in the XRD patterns of all samples was nesquehonite, with three peaks located at 13.6°, 23.1° and 29.4° (2θ) [56]. By comparing the intensities of peaks on the XRD patterns at 7 d and 14 d, a reduction in the brucite and an increase in nesquehonite peaks were observed. This revealed the carbonation of brucite to form nesquehonite from 7 d to 14 d, which was generally in line with the Raman results. However, the peaks for hydromagnesite could not be observed in Fig. 8, which could be due to the relatively low crystallization degree [57].

The XRD patterns of carbonated brucite at different ages of carbonation are shown in Fig. 8. The main peaks were located at 18.1°, 38.0° (2θ), along with the peaks at 50.8°, 58.6° 62.1° and 68.2° (2θ), corresponding to the presence of brucite as the major phase [54,55]. The main HMC was found to be hydromagnesite, evidenced by the peaks at

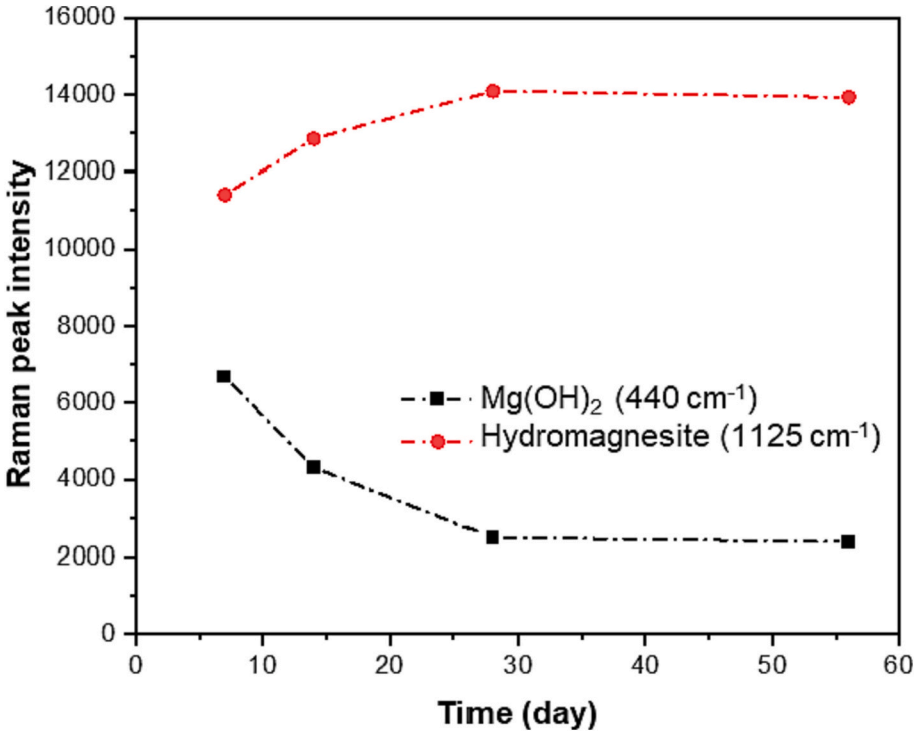

Fig. 7. Evolution of the Raman peaks intensities of carbonated brucite cement at 440 and 1125 cm^{-1} with time.

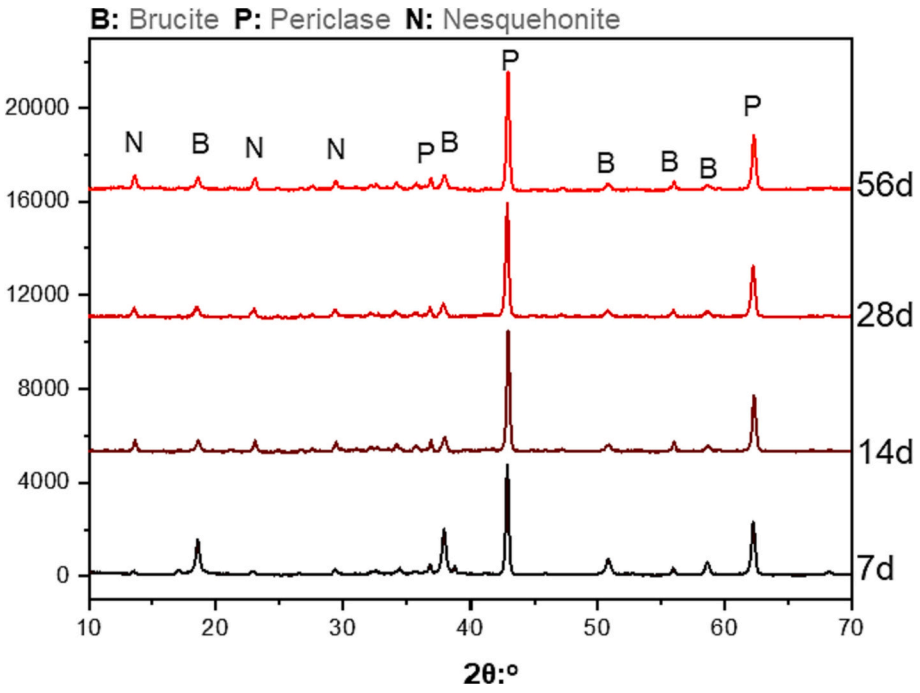

Fig. 8. XRD patterns of carbonated RMC after 7 d, 14 d, 28 d and 56 d of carbonation.

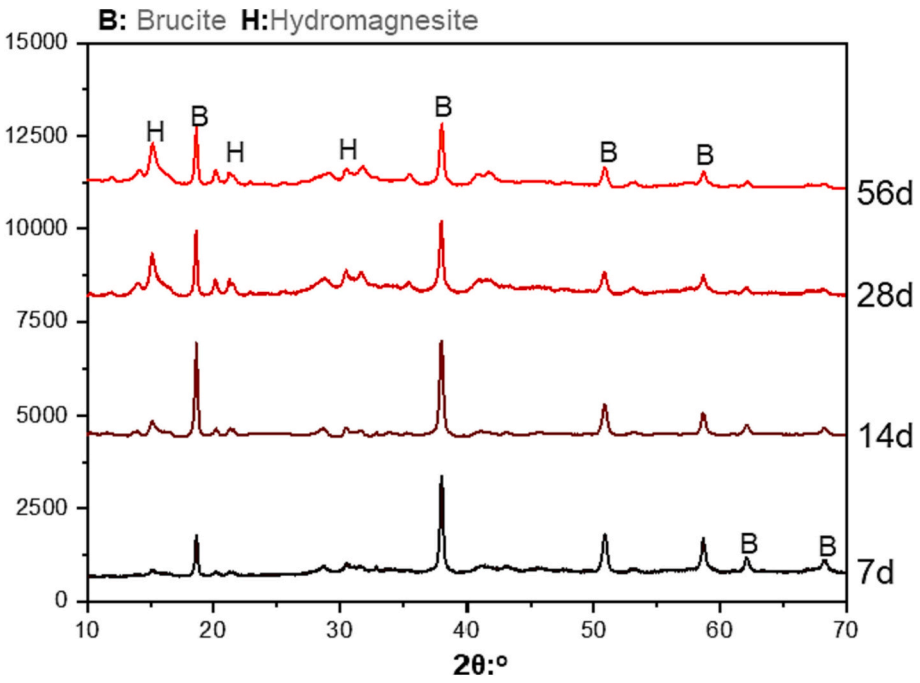

Fig. 9. XRD patterns of carbonated brucite after 7 d, 14 d, 28 d and 56 d of carbonation.

15.2°, 21.2° and 30.5° (2θ) [58]. There was a reduction in the peak intensities of brucite as carbonation progressed over time, whilst the peak intensities of hydromagnesite increased constantly until 28 d. The XRD patterns at 28 d and 56 d were comparable, indicating the absence of any noticeable changes to carbonation after 28 d.

Overall, the results obtained in XRD revealed the main HMCs as nesquehonite and hydromagnesite in carbonated RMC and brucite cement, respectively. The findings also demonstrated the completion of the carbonation reaction under the conditions provided at 28 d. These findings were generally consistent with those observed from Raman results.

3.1.3. Scanning electron microscopy (SEM) results

The SEM images of carbonated RMC and brucite cement are presented in Fig. 10. The morphology of carbonated RMC mainly consisted of needle-like nesquehonite [59], along with rosette-like hydromagnesite [20], as labelled in Fig. 10 (a)–(c). These observations were aligned with those reported in the literature [9,20]. Alternatively, the needle-like nesquehonite was absent in carbonated brucite cement, as shown in Fig. 10 (d)–(f), where the main HMC phase was identified as hydromagnesite. The co-existence of the 2 HMCs (nesquehonite and hydromagnesite) in carbonated RMC was consistent with Raman results. The observation of hydromagnesite in carbonated brucite cement was

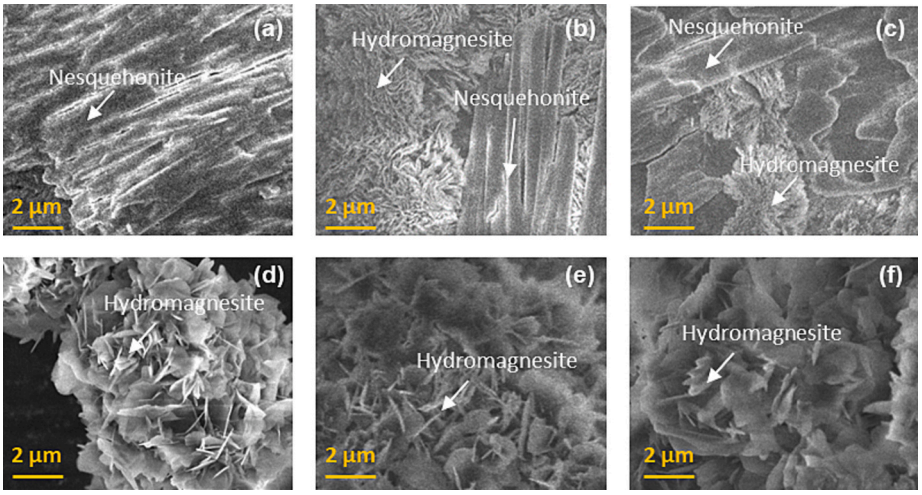

Fig. 10. SEM images of (a)–(c) RMC and (d)–(f) brucite cement after 28 d of carbonation.

also in line with the XRD and Raman results.

3.2. Establishing correlations for the quantification of carbonation in RMC and brucite cements by Raman spectroscopy

Correlations between Raman peak intensities and corresponding carbonation degrees in different Mg-based systems listed in Table 1 were established via Raman mapping. Considering that the 2 main HMC phases observed in these samples were nesquehonite and hydromagnesite, the intensities of corresponding Raman peaks at 1100 cm^{-1} and 1125 cm^{-1} were selected as the indicators of carbonation degree. The intensities of these peaks were converted into carbonation degree (%) as a reference for future evaluation of the carbonation behaviour of RMC and brucite cements. It is important to highlight that the carbonation degree of both the carbonated RMC and brucite was assumed to be 100 % in present work as explained earlier since subsequent carbonation was minimally observed under the accelerated carbonation conditions.

The spot size of the laser was approximately 4 μm, which could encompass a considerable area relative to a single crystal. Though the crystallinity of the phases had an impact on the Raman peak intensity, it is impractical to account for the crystallization degree of each individual crystal. Therefore, the quantification analysis in the present work was based on the statistical outcomes derived from testing 135 points for each type of standard sample, irrespective of the crystallization degree of individual crystals. Substantially, the underlying concept revolved around predicting the most probable Raman peak intensity associated with different degrees of carbonation. Overall, the establishment of the correlation between the Raman peak intensity and carbonation degree was based on a comprehensive dataset comprising total of 810 test points, which incorporated statistical analyses of reference samples with varying carbonation degrees.

3.2.1. Carbonated RMC

Fig. 11 (a) shows the Raman mapping results obtained from RMC reference samples with different colours indicating the variations in Raman peak intensities at ~1100 cm^{-1}, i.e. the characteristic peak of nesquehonite. When there was an absence of carbonated RMC, i.e. carbonation degree was 0 %, the maps were all in blue, revealing that almost no nesquehonite existed. With an increase of carbonate RMC content, the mapping results initially turned to red and eventually became dark red when the content was up to 100 %. Intensities higher than 6000 were depicted in dark red colour.

Based on the variations observed in the mapping results, it can be derived that the intensity of the Raman peak was correlated to the carbonation degree of RMC. To establish a clear correlation between the Raman intensity at 1100 cm^{-1} and carbonation degree (i.e. the content of carbonated RMC), the Raman peak intensities of every test point were further plotted as a box chart in Fig. 11 (b). Raman peak intensity had a linear correlation with the amount of the chemical compounds under the measurement [36,60]. Based on the data points, a linear relationship between the carbonation degree and Raman peak intensities at ~1100 cm^{-1} was illustrated with a red dash line. The obtained fitting line followed Eq. (1).

$$y_{Rn} = 324 + 4657x_{Rn}\left(r^2 = 0.85; RMSE = 1016\right) \quad (1)$$

(where x_{Rn} is the carbonation degree based on the Raman peak at ~1100 cm^{-1}; y_{Rn} is the intensity of this Raman peak; and RMSE is the root mean square error.)

Similarly, the Raman mapping results and box chart for the Raman peak at ~1125 cm^{-1}, the characteristic peak of hydromagnesite, are shown in Fig. 12. Based on the differences in the mapping results, it was observed that the intensity of the Raman peak at ~1125 cm^{-1} increased with an increase in the carbonation degree, showing a similar trend to that observed for the Raman peak at ~1100 cm^{-1}. Intensities surpassing 2000 were visualized using a dark green colour. The linear correlation between the Raman peak intensities at ~1125 cm^{-1} and the carbonation degree are established in Fig. 12 (b). By regression analysis of all data points, the line of best fit was drawn as a dashed red line in the plot with a formula shown in Eq. (2).

$$y_{Rh} = 268 + 1535x_{Rh}\left(r^2 = 0.81; RMSE = 392\right) \quad (2)$$

(where x_{Rn} is the carbonation degree based on the Raman peak at ~1125 cm^{-1}; y_{Rh} is the intensity of this Raman peak; and RMSE is the root mean square error.)

3.2.2. Carbonated brucite cement

Fig. 13 (a) shows the Raman mapping results of the carbonated brucite cement samples for the peak at 1125 cm^{-1}. A constant increase in the peak intensities was observed with an increase of the carbonation degree from 0 % to 100 %, which was evidenced by the gradual change in the colour in most areas of the mapping results towards dark blue. Intensities above 15,000 were depicted in dark blue colour. This was in line with the earlier findings reporting an increase in the hydromagnesite content as carbonation progressed over time. All data points are plotted as a box chart in Fig. 13 (b). Based on these data points, a linear correlation between Raman peak intensities at 1125 cm^{-1} and the carbonation degree of brucite cement was established. Accordingly, a fitting line with a formula shown in Eq. (3) was obtained.

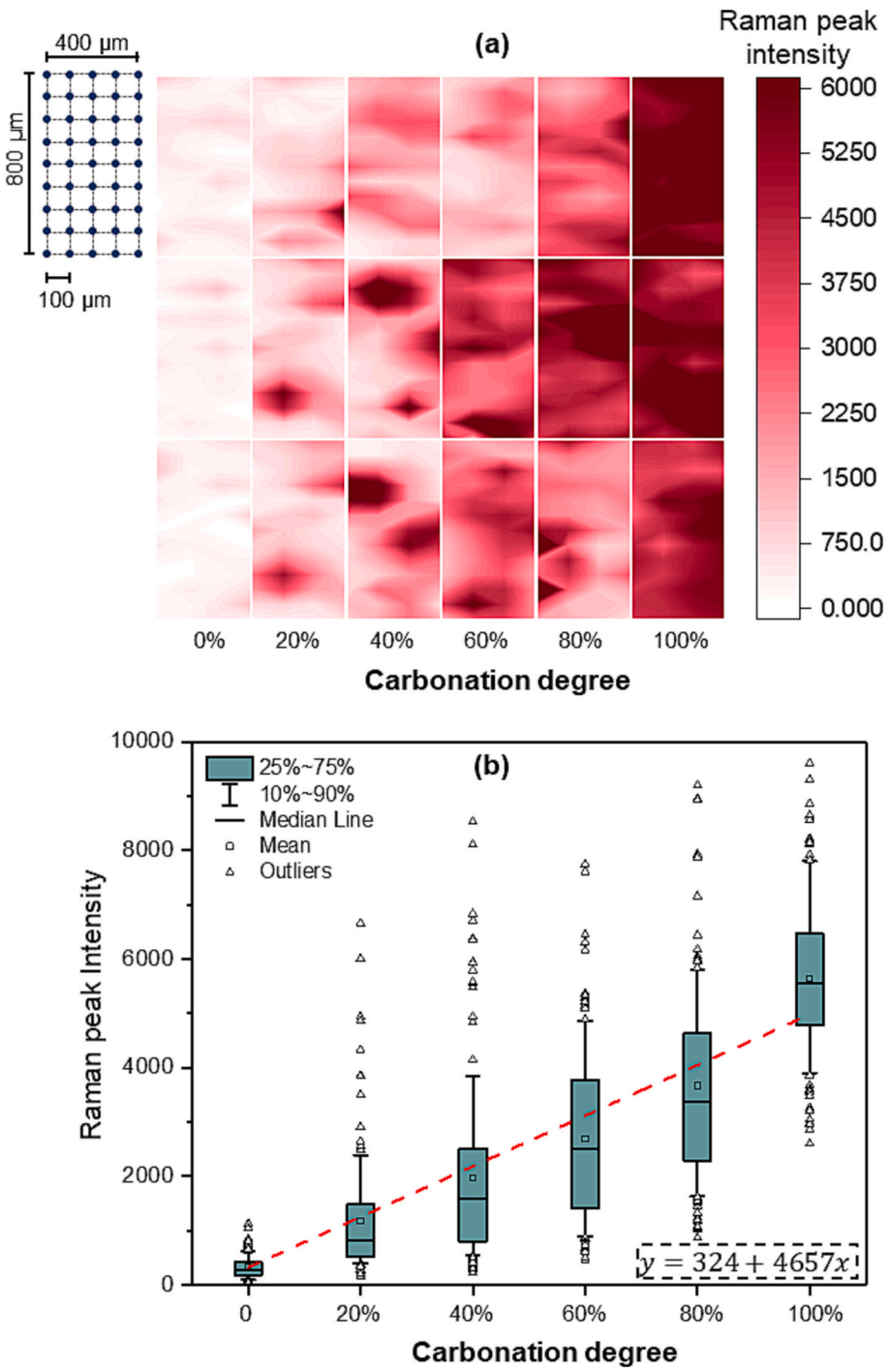

Fig. 11. (a) The Raman mapping results (obtained from a matrix of 5 × 9 in a range of 400 × 800 μm, i.e. 135 (45 × 3) data points for each sample) of carbonated RMC based on the Raman peaks at 1100 cm^{-1}, and (b) box plot of Raman peak intensities at 1100 cm^{-1} (corresponding to nesquehonite) against the carbonation degree of RMC.

$$y_b = 317 + 13267x_b \ \left(r^2 = 0.92; RMSE = 2509\right) \quad (3)$$

(where x_b is the carbonation degree of brucite cement; y_b is the intensity of the Raman peak at 1125 cm^{-1} obtained from carbonated brucite cement; and RMSE is the root mean square error.)

3.3. Quantification of carbonated RMC and brucite cements based on the established correlations

The correlations established in Section 3.2 were used in performing quantitative analysis of carbonated RMC and brucite cements in this section. A systematic averaging process was employed at each depth to effectively mitigate the impact of sporadic high intensity occurrences. The depth of carbonation, also known as the carbonation front [61], denoted the position where the carbonation degree equalled zero.

3.3.1. Quantification of carbonated RMC

RMC cement exposed to carbonation for 3 d and 7 d was evaluated by Raman spectroscopy. Fig. 14 (a) shows the Raman mapping results, which present the distribution of nesquehonite and hydromagnesite and

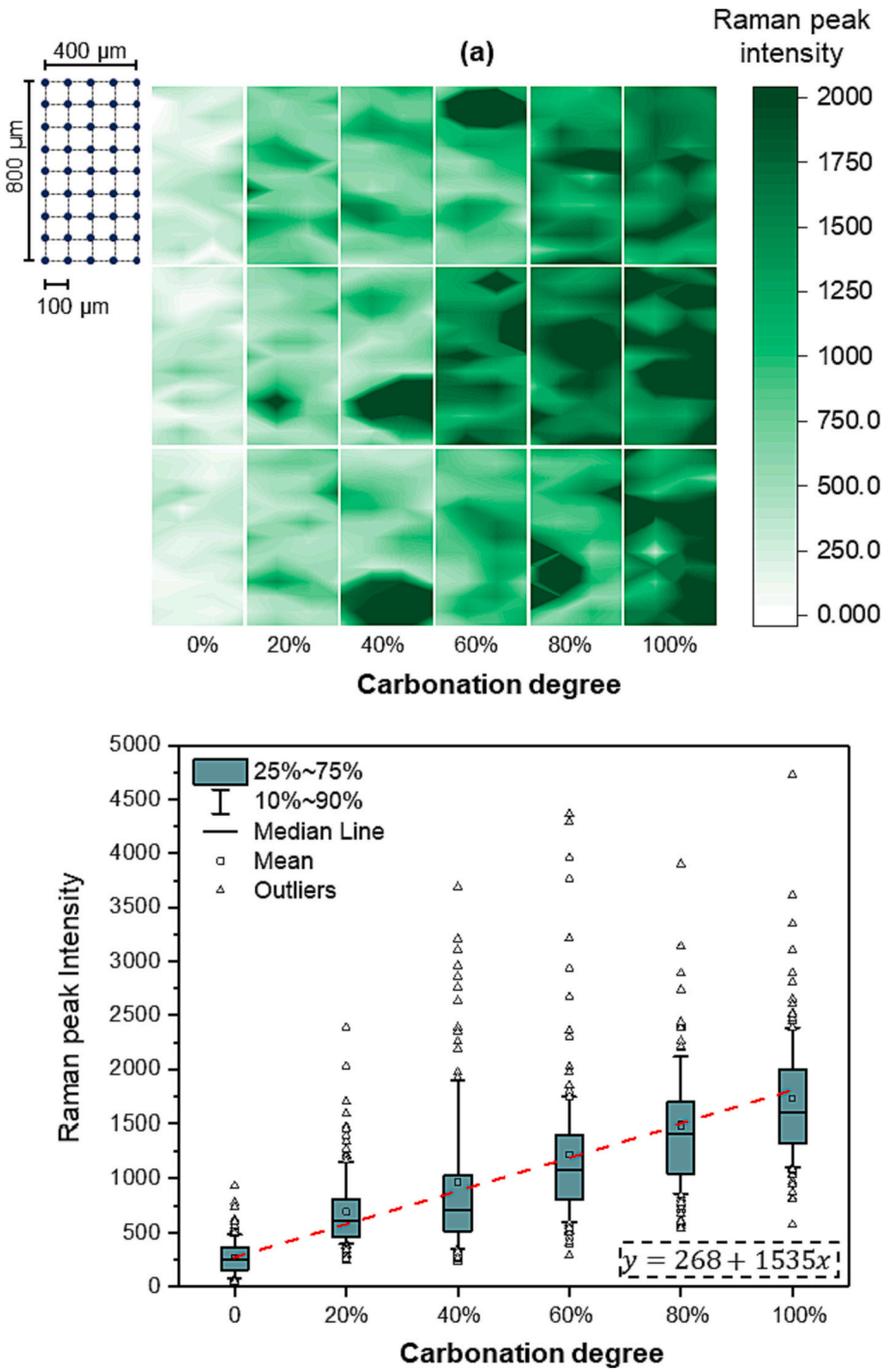

Fig. 12. (a) The Raman mapping results (obtained from a matrix of 5 × 9 in a range of 400 × 800 μm, i.e. 135 (45 × 3) data points for each sample) of carbonated RMC based on the Raman peaks at 1125 cm^{-1}, and (b) box plot of Raman peak intensities at 1125 cm^{-1} (corresponding to hydromagnesite) against carbonation degree of RMC.

their relative amounts in terms of carbonation degree. Generally, both the fully carbonated (red) and partially carbonated (green) areas increased significantly from 3 d to 7 d, indicating the constant penetration of CO_2 during carbonation curing at early stages.

To further quantify the carbonation degree of RMC after 3 d and 7 d, the scattering plot of the carbonation degree of RMC at different depths are provided in Fig. 14 (b) and (c) according to the Raman mapping results shown in Fig. 14 (a). In general, the carbonation degrees linked with the presence of nesquehonite and hydromagnesite both increased with time at all depths. In terms of the carbonation depth, the results indicated by nesquehonite and hydromagnesite were comparable, revealing a depth of ~1.1 mm at 3 d of carbonation and ~3 mm at 7 d. However, the fully carbonated zone (i.e. referring to the area with a carbonation degree of 100 %) indicated by hydromagnesite was deeper than that indicated by nesquehonite, which revealed that hydromagnesite formation took place at higher sample depths.

However, as carbonation progressed to higher depths, the transformation dynamics became complex. Several factors such as the reaction kinetics, mineral availability, and the interplay of various factors during the carbonation process need to be considered. Eqs. (4) and (5)

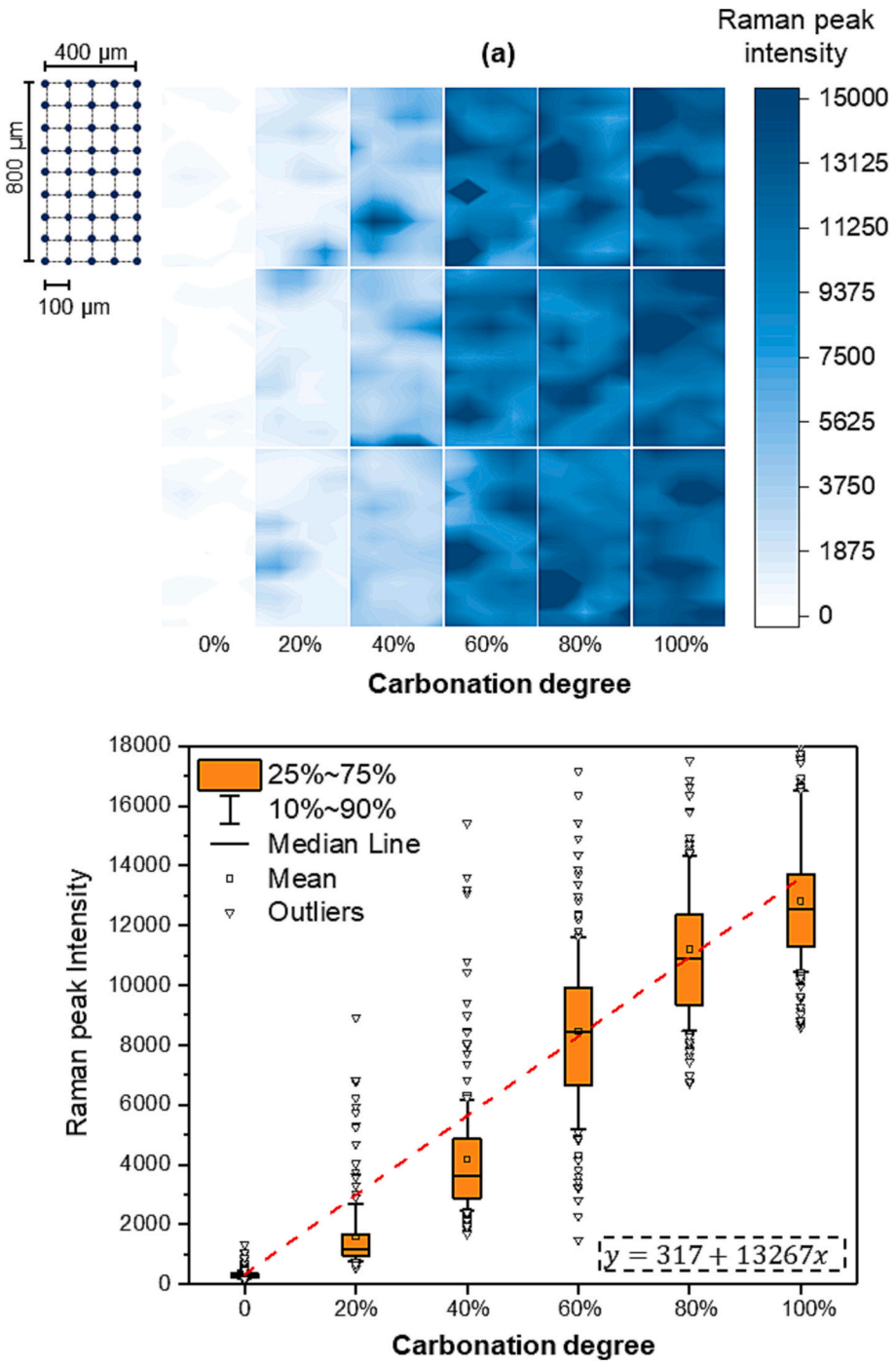

Fig. 13. (a) The Raman mapping results (obtained from a matrix of 5 × 9 in a range of 400 × 800 μm, i.e. 135 (45 × 3) data points for each sample) of carbonated brucite cement based on the Raman peaks at 1125 cm^{-1}, and (b) box plot of Raman peak intensities at 1125 cm^{-1} (corresponding to hydromagnesite) against carbonation degree of brucite cement.

show the formation of nesquehonite and hydromagnesite [4,28], whilst their transformation is demonstrated in Eq. (6). Accordingly, the formation of nesquehonite/hydromagnesite could result from either the direct carbonation of $Mg(OH)_2$ or the transformation of other phases. Although hydromagnesite was reported to be thermodynamically more stable [62], the transformation between nesquehonite and hydromagnesite is a dynamic process depending on the availability of reactants, such as $Mg(OH)_2$ or H_2O. At higher depths, the increased availability of $Mg(OH)_2$ may promote the formation of hydromagnesite, which could explain the results obtained in this study.

$$Mg(OH)_2 + CO_2 + 2H_2O \rightarrow MgCO_3 \bullet 3H_2O \text{ (nesquehonite)} \quad (4)$$

$$5Mg(OH)_2 + 4CO_2 \rightarrow 4MgCO_3 \bullet Mg(OH)_2 \bullet 4H_2O \text{ (hydromagnesite)} \quad (5)$$

$$4(MgCO_3 \bullet 3H_2O) + Mg(OH)_2 \leftrightarrow 4MgCO_3 \bullet Mg(OH)_2 \bullet 4H_2O + 8H_2O \quad (6)$$

3.3.2. Quantification of carbonated brucite cement

Fig. 15 shows the Raman mapping results of carbonated brucite cement after 3 d and 7 d of carbonation curing. According to Fig. 15 (a),

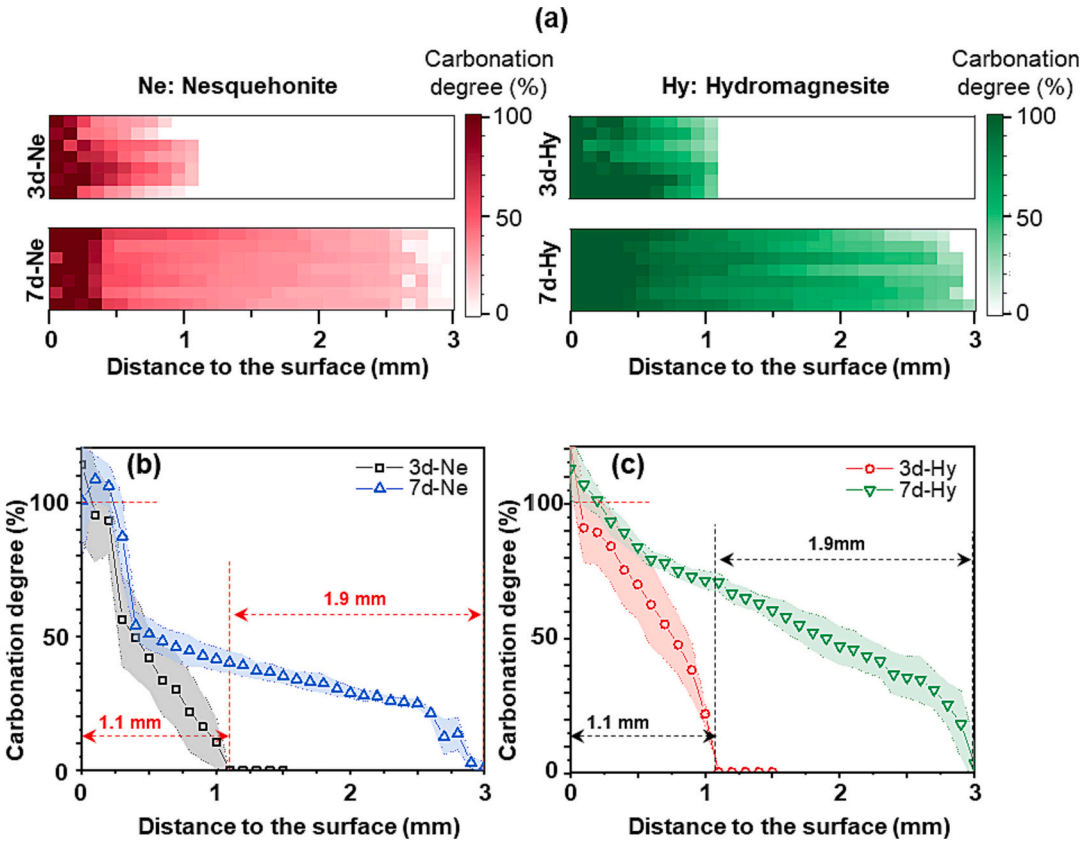

Fig. 14. (a) Raman heatmap results of RMC after carbonation, and scatter plots of the carbonation degree at different depths according to the Raman mapping results, indicated by (b) nesquehonite and (c) hydromagnesite.

carbonation degree decreased with an increase in sample depth, which was attributed to the reduction in the accessibility (i.e. limited diffusion) of CO_2 at higher depths. The increase in carbonation depth and degree from 3 d to 7 d indicated the progress in carbonation reaction over this period. To clearly quantify the carbonation depth and degree, Fig. 15 (b) shows the scattering plot of the carbonation degree at different depths based on the results demonstrated in Fig. 15 (a). Accordingly, the carbonation degree of brucite cement at the surface was only ~50 % at 3 d, which increased to ~65 % at 7 d. Therefore, the surface of the brucite cement was not fully carbonated after 7 d of exposure to accelerated carbonation, which was possibly due to 1) the low dissolution rate of brucite [63], 2) the surface passivation of brucite owing to precipitation of HMCs [64], and 3) the limited carbonation duration (i.e. as opposed to the 28 d of carbonation used earlier in Section 3.1). Accordingly, the carbonation depth increased from 2.5 mm at 3 d to 3 mm at 7 d as shown in Fig. 15 (b). When compared to the carbonation depth of RMC shown in Fig. 14 (b and c), carbonated brucite cement demonstrated a higher carbonation depth initially at 3 d, reaching comparable values at 7 d.

4. Discussion

The work presented in this study identified the differences in the carbonation products formed in carbonated RMC and brucite cements, which was generally in line with those reported in the literature [4,5,9,18–24]. In RMC systems, reactive MgO was firstly hydrated to form $Mg(OH)_2$ which was then carbonated to form HMCs [65]. However, the hydration degree of RMC was limited due to its low rate of dissolution and the precipitation of hydration and carbonation products on the surface of unhydrated MgO particles [12]. Therefore, the amount of hydrate phase ($Mg(OH)_2$) available in RMC was less than that in brucite cement. As a consequence, owing to the larger amount of $Mg(OH)_2$ available, the formation of hydromagnesite was promoted in brucite cement.

Alternatively, nesquehonite was found to be the major HMCs in carbonated RMC, along with hydromagnesite. The crystal structures of brucite, nesquehonite and hydromagnesite, as shown in Fig. 16, could further support these findings. Accordingly, in all three structures, the Mg atom is surrounded by six oxygen atoms to form a MgO_6 octahedral structure. Brucite consists of sheets of MgO_6 octahedra with H atoms at each apex [66], whilst the Mg atom in nesquehonite is coordinated by four oxygen atoms from carbonates and two from water molecules [67]. Different from nesquehonite, one of the oxygen atoms from the water molecule is replaced by a hydroxyl ion in hydromagnesite [68]. Therefore, the existence of abundant hydroxyl ions could promote the transformation from nesquehonite to hydromagnesite. Similarly, previous studies reported that a higher pH value, i.e. more hydroxyl ions, could advance the formation of hydromagnesite from nesquehonite [16,17]. Therefore, the availability of $Mg(OH)_2$, i.e. the amount of hydroxyl ions, could play a role in the formation of different "dominant" carbonation products in RMC and brucite cements.

This study also revealed the differences between the findings obtained by two techniques, XRD and Raman spectroscopy. With the same amount of HMCs in samples, Raman spectra (Figs. 4 and 6) presented much sharper peaks, i.e. more intense signal, than those shown in the XRD patterns (Figs. 8 and 9). This difference could be caused by the variation in the principles of each technique. Raman spectroscopy is based on the vibration modes of the chemical bonds, where the peak intensity corresponds to the amount of substrate with certain chemical bonds [38]. XRD is based on constructive interference of X-rays and a crystalline sample, whilst the peak intensity of the XRD pattern is associated with the crystallization degree of the substrate [57]. The newly formed nesquehonite and hydromagnesite were reported to have poor crystallinity, especially those forming at early stages [4,71,72], which are thus likely to induce relatively weak peaks in the XRD

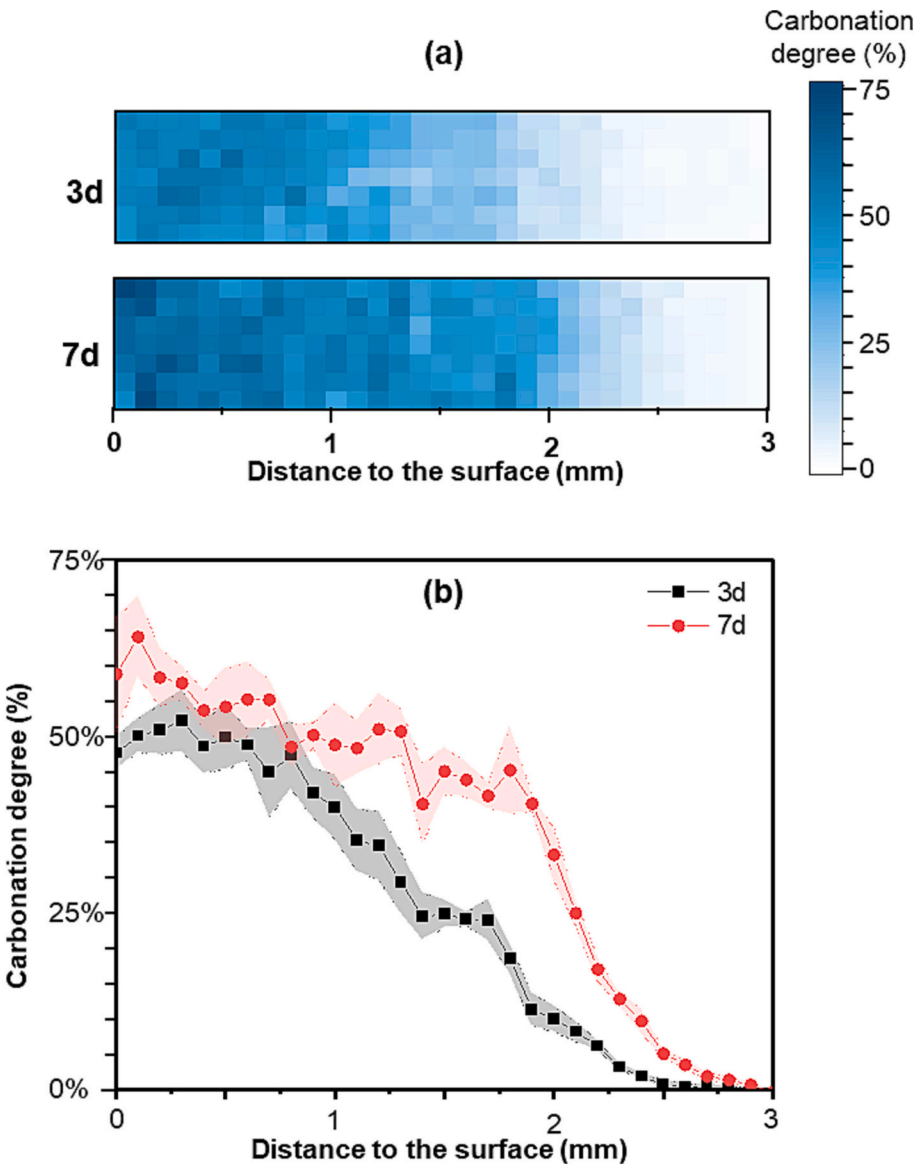

Fig. 15. (a) Raman heatmap results of the brucite cement after carbonation and (b) scatter plot of the carbonation degree at different depths based on the Raman mapping results.

patterns. Therefore, the peaks for hydromagnesite were not observed in Fig. 8. Alternatively, the C—O bond in nesquehonite and hydromagnesite could be identified easily by Raman spectroscopy, as evidenced in Figs. 4 and 6. Therefore, it can be concluded that Raman spectroscopy is more sensitive to detect different HMCs that form in carbonated RMC and brucite cements. This becomes particularly important at early stages of carbonation, at which state a limited amount of HMCs, with relatively poor crystallinities, form. In these scenarios, Raman spectroscopy has demonstrated its suitability in the identification and further evaluation of the carbonation of different Mg-based systems.

Pixel counting has proven to be a valuable practice for gaining insights into carbonation, as demonstrated in previous studies [39–42]. However, pixel counting is more suitable in the presence of a substantial number of test points, as reported in previous studies [42], where around 241,000 test points were acquired in a Raman mapping measurement. Though this approach could yield high resolution chemical imaging, its practicality for future engineering applications is questionable due the long analysis durations. In contrast, the current study employs a different methodology to quantify carbonation, which integrating both pixel counting and pixel intensity.

Compared with solely pixel counting, the present work further established the carbonation degree and Raman peak intensities by employing reference samples with fitted carbonation degrees. With a longer total accumulation time (10 s) compared to the literature's customary duration (commonly <1 s) [39–42], the sensitivity of the Raman peak intensity corresponding to the carbonation degree was significantly enhanced. Consequently, a correlation between the Raman peak intensity and carbonation degree was established based on the statistical analyses of the Raman results of the reference samples.

In addition to the Raman intensity, pixel counting was also incorporated in the current work. The statistical analyses presented in Figs. 11–13 involved pixel counting at various intensities, yielding a correlation between pixel intensity and carbonation degree. However, a 4 μm spot may encompass multiple particles/phases, leading to variations in intensity. Additionally, the heterogeneity of cement carbonation, as evidenced in prior studies [36,40], enhanced the complexity of the interpretation of single spot measurements at this spatial scale. Consequently, they may not precisely reflect the carbonation degree of the whole sample based on a single spot measurement. Therefore, the

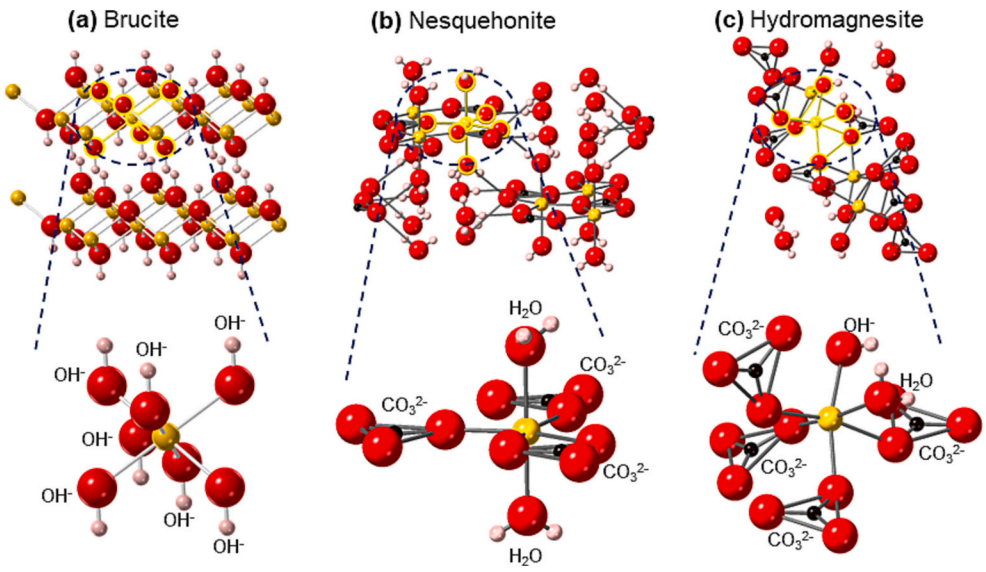

Fig. 16. Molecular structures of (a) brucite [69], (b) nesquehonite [67] and (c) hydromagnesite [70].

assessment of carbonation degree at a particular depth involved examining 7 pixels at a consistent depth, as depicted in the scatter plots of Figs. 14 (b), (c) and 15 (b). This approach effectively mitigated intensity variations across diverse locations by utilizing the averaged intensity value derived from these 7 pixels. Alternatively, the direct translation of Raman intensity into carbonation degree aimed to represent the local carbonation condition at a single spot, a measure not directly indicative of the overall carbonation degree of the entire sample. To evaluate the carbonation degree of the whole sample, the carbonation degree of all spots should be considered via the use of both pixel counting and pixel intensity.

5. Conclusion

The present work demonstrated the use of Raman spectroscopy in the identification of the different phases that form and quantification of the carbonation of RMC and brucite-based cements. Correlations between the Raman peaks and carbonation degree were established based on the Raman mapping results of reference samples. Furthermore, the feasibility of employing the established correlations was demonstrated. The main findings emerging from this study were as follows:

- The dominant carbonation products of RMC and brucite-based cements were nesquehonite and hydromagnesite, respectively. The carbonation of both systems was completed by 28 days under accelerated carbonation conditions (30 °C, 80 % RH, and 20 % CO_2 concentration) in powder form.
- When compared with XRD, Raman spectroscopy revealed a higher sensitivity in the detection of different carbonation products at early stages, which was especially evident in RMC samples.
- Correlations between the Raman peaks and carbonation degree were established for both RMC and brucite-based cements, which were all linear with an R value over 0.9.
- The established correlations were successfully employed to evaluate the carbonation behaviour of RMC and brucite cements under carbonation curing conditions. Critical information, such as carbonation depth, carbonation degree and the distribution of different carbonation products was obtained.

In conclusion, the Raman results not only revealed the degree of carbonation at different depths but also the distribution of different carbonation products and their amounts at different durations in the two Mg-based binder systems (Figs. 14 and 15). This information can be used to evaluate the strength and microstructural development of RMC- and brucite-based cements since (1) different types of HMCs have various densities and morphologies, inducing different interlocking effects and performance contributions, (2) a higher carbonation depth is generally beneficial for strength development, and (3) transformation of different HMCs from one form to another can influence the overall performance of the final product.

Building upon this demonstration of using Raman spectroscopy, the outcome of this present work could not only contribute to advancing the understanding of the carbonation mechanisms and associated strength development of different Mg-based systems, but also enable the prediction of the carbonation degree and evaluation of performance within these samples via the established correlations. Raman spectroscopy proved instrumental in quantitatively assessing carbonation products, monitoring their temporal depth and distribution, and establishing correlations with mechanical properties for the refinement of Mg-based cements. Moreover, this analytical method can facilitate quality control and predictive modelling; and foster the development of sustainable practices involving Mg-based cements.

CRediT authorship contribution statement

Tangwei Mi: Writing – review & editing, Writing – original draft, Validation, Methodology, Investigation, Formal analysis, Conceptualization. **Xi Chen:** Writing – original draft, Validation, Investigation, Formal analysis. **En-Hua Yang:** Writing – review & editing, Writing – original draft, Supervision, Resources, Project administration, Methodology, Conceptualization. **Cise Unluer:** Writing – review & editing, Writing – original draft, Supervision, Resources, Project administration, Methodology, Conceptualization.

Declaration of competing interest

The authors declare that there is no known conflict of interest.

Data availability

No data was used for the research described in the article.

Acknowledgements

The authors would like to acknowledge financial support from the Ministry of National Development, Singapore (CoT-V1-2020-1).

Appendix A. Supplementary data

Supplementary data to this article can be found online at https://doi.org/10.1016/j.cemconres.2024.107454.

References

[1] E. Gartner, Industrially interesting approaches to "low-CO2" cements, Cem. Concr. Res. 34 (2004) 1489–1498.
[2] R. Maddalena, J.J. Roberts, A. Hamilton, Can Portland cement be replaced by low-carbon alternative materials? A study on the thermal properties and carbon emissions of innovative cements, J. Clean. Prod. 186 (2018) 933–942.
[3] U.N. Environment, K.L. Scrivener, V.M. John, E.M. Gartner, Eco-efficient cements: potential, economically viable solutions for a low-CO2 cement based industry, Cem. Concr. Res. 114 (2018) 2–26.
[4] I. Singh, R. Hay, K. Celik, Recovery and direct carbonation of brucite from desalination reject brine for use as a construction material, Cem. Concr. Res. 152 (2022) 106673.
[5] S. Ruan, E.-H. Yang, C. Unluer, Production of reactive magnesia from desalination reject brine and its use as a binder, J. CO2 Util. 44 (2021) 101383.
[6] H. Dong, C. Unluer, E.-H. Yang, A. Al-Tabbaa, Recovery of reactive MgO from reject brine via the addition of NaOH, Desalination 429 (2018) 88–95.
[7] H. Dong, C. Unluer, E.-H. Yang, A. Al-Tabbaa, Synthesis of reactive MgO from reject brine via the addition of NH4OH, Hydrometallurgy 169 (2017) 165–172.
[8] C. Sonat, C.H. Lim, M. Liska, C. Unluer, Recycling and reuse of reactive MgO cements – a feasibility study, Construct. Build Mater. 157 (2017) 172–181.
[9] N.T. Dung, R. Hay, A. Lesimple, K. Celik, C. Unluer, Influence of CO2 concentration on the performance of MgO cement mixes, Cem. Concr. Compos. 115 (2021) 103826.
[10] M. Liska, A. Al-Tabbaa, K. Carter, J. Fifield, Scaled-up commercial production of reactive magnesium cement pressed masonry units. Part I: production, Proc. Inst. Civil Eng.-Construct. Mater. 165 (2012) 211–223.
[11] M. Liska, A. Al-Tabbaa, K. Carter, J. Fifield, Scaled-up commercial production of reactive magnesia cement pressed masonry units. Part II: performance, Proc. Inst. Civil Eng.-Construct. Mater. 165 (2012) 225–243.
[12] N.T. Dung, C. Unluer, Development of MgO concrete with enhanced hydration and carbonation mechanisms, Cem. Concr. Res. 103 (2018) 160–169.
[13] N.T. Dung, C. Unluer, Improving the carbonation of reactive MgO cement concrete via the use of NaHCO3 and NaCl, J. Mater. Civ. Eng. 30 (2018) 04018320.
[14] A. Botha, C.A. Strydom, Preparation of a magnesium hydroxy carbonate from magnesium hydroxide, Hydrometallurgy 62 (2001) 175–183.
[15] E. Königsberger, L.-C. Königsberger, H. Gamsjäger, Low-temperature thermodynamic model for the system Na2CO3−MgCO3−CaCO3−H2O, Geochim. Cosmochim. Acta 63 (1999) 3105–3119.
[16] Z. Zhang, Y. Zheng, Y. Ni, Z. Liu, J. Chen, X. Liang, Temperature-and pH-dependent morphology and FT− IR analysis of magnesium carbonate hydrates, J. Phys. Chem. B. 110 (2006) 12969–12973.
[17] L. Hopkinson, P. Kristova, K. Rutt, G. Cressey, Phase transitions in the system MgO–CO2–H2O during CO2 degassing of Mg-bearing solutions, Geochim. Cosmochim. Acta 76 (2012) 1–13.
[18] R. Hay, N.T. Dung, A. Lesimple, C. Unluer, K. Celik, Mechanical and microstructural changes in reactive magnesium oxide cement-based concrete mixes subjected to high temperatures, Cem. Concr. Compos. 118 (2021) 103955.
[19] C. Unluer, A. Al-Tabbaa, Impact of hydrated magnesium carbonate additives on the carbonation of reactive MgO cements, Cem. Concr. Res. 54 (2013) 87–97.
[20] N.T. Dung, A. Lesimple, R. Hay, K. Celik, C. Unluer, Formation of carbonate phases and their effect on the performance of reactive MgO cement formulations, Cem. Concr. Res. 125 (2019) 105894.
[21] S. Kumar, E.-H. Yang, C. Unluer, Investigation of chloride penetration in carbonated reactive magnesia cement mixes exposed to cyclic wetting–drying, Construct. Build Mater. 284 (2021) 122837.
[22] K. Rausis, A. Ćwik, I. Casanova, Phase evolution during accelerated CO2 mineralization of brucite under concentrated CO2 and simulated flue gas conditions, J. CO2 Util. 37 (2020) 122–133.
[23] X. Zhang, A.S. Lea, A.M. Chaka, J.S. Loring, S.T. Mergelsberg, E. Nakouzi, O. Qafoku, J.J. De Yoreo, H.T. Schaef, K.M. Rosso, In situ imaging of amorphous intermediates during brucite carbonation in supercritical CO2, Nat. Mater. 21 (2022) 345–351.
[24] H.T. Schaef, C.F. Windisch, B.P. McGrail, P.F. Martin, K.M. Rosso, Brucite [Mg (OH2)] carbonation in wet supercritical CO2: an in situ high pressure X-ray diffraction study, Geochim. Cosmochim. Acta 75 (2011) 7458–7471.
[25] L. Mo, F. Zhang, M. Deng, D.K. Panesar, Effectiveness of using CO2 pressure to enhance the carbonation of Portland cement-fly ash-MgO mortars, Cem. Concr. Compos. 70 (2016) 78–85.
[26] D.K. Panesar, L. Mo, Properties of binary and ternary reactive MgO mortar blends subjected to CO2 curing, Cem. Concr. Compos. 38 (2013) 40–49.
[27] L. Pu, C. Unluer, Investigation of carbonation depth and its influence on the performance and microstructure of MgO cement and PC mixes, Construct. Build Mater. 120 (2016) 349–363.
[28] T. Hoang, N.T. Dung, C. Unluer, J. Chu, Use of microbial carbonation process to enable self-carbonation of reactive MgO cement mixes, Cem. Concr. Res. 143 (2021) 106391.
[29] R. Hay, K. Celik, Hydration, carbonation, strength development and corrosion resistance of reactive MgO cement-based composites, Cem. Concr. Res. 128 (2020) 105941.
[30] R. Hay, B. Peng, K. Celik, Filler effects of CaCO3 polymorphs derived from limestone and seashell on hydration and carbonation of reactive magnesium oxide (MgO) cement (RMC), Cem. Concr. Res. 164 (2023) 107040.
[31] C. Unluer, A. Al-Tabbaa, The role of brucite, ground granulated blastfurnace slag, and magnesium silicates in the carbonation and performance of MgO cements, Construct. Build Mater. 94 (2015) 629–643.
[32] C.-F. Chang, J.-W. Chen, The experimental investigation of concrete carbonation depth, Cem. Concr. Res. 36 (2006) 1760–1767.
[33] D. Meng, C. Unluer, E.-H. Yang, S. Qian, Recent advances in magnesium-based materials: CO2 sequestration and utilization, mechanical properties and environmental impact, Cem. Concr. Compos. 138 (2023) 104983.
[34] K. Cho, C. Kim, Enhanced mineral carbonation at room temperature through MgO nanocubes synthesized by self-combustion, J. Environ. Chem. Eng. 9 (2021) 105592.
[35] T. Mi, Y. Li, W. Liu, Z. Dong, Q. Gong, C. Min, F. Xing, Y. Wang, S.H. Chu, The effect of carbonation on chloride redistribution and corrosion of steel reinforcement, Construct. Build Mater. 363 (2023) 129641.
[36] T. Mi, Y. Li, W. Liu, W. Li, W. Long, Z. Dong, Q. Gong, F. Xing, Y. Wang, Quantitative evaluation of cement paste carbonation using Raman spectroscopy, NPJ Mater. Degrad. 5 (2021) 35.
[37] R. Hay, K. Celik, Accelerated carbonation of reactive magnesium oxide cement (RMC)-based composite with supercritical carbon dioxide (scCO2), J. Clean. Prod. 248 (2020) 119282.
[38] D.A. Long, Raman Spectroscopy, McGraw-Hill, New York, 1977.
[39] D. Stefaniuk, M. Hajduczek, J.C. Weaver, F.J. Ulm, A. Masic, Cementing CO2 into CSH: a step toward concrete carbon neutrality, PNAS Nexus 2 (2023) pgad052.
[40] S. Srivastava, N. Garg, Tracking spatiotemporal evolution of cementitious carbonation via Raman imaging, J. Raman Spectrosc. 54 (2023) 414–425.
[41] K. Zhang, M. Yio, H. Wong, N. Buenfeld, Real-time monitoring of carbonation of hardened cement pastes using Raman microscopy, J. Microsc. 286 (2022) 126–133.
[42] K. Zhang, M. Yio, H. Wong, N. Buenfeld, Development of more accurate methods for determining carbonation depth in cement-based materials, Cem. Concr. Res. 175 (2024) 107358.
[43] M. Torres-Carrasco, A. del Campo, M. de la Rubia, E. Reyes, A. Moragues, J. Fernández, New insights in weathering analysis of anhydrous cements by using high spectral and spatial resolution confocal Raman microscopy, Cem. Concr. Res. 100 (2017) 119–128.
[44] K. Zhang, M.H.N. Yio, H.S. Wong, N.R. Buenfeld, Optimising confocal Raman microscopy for spectral mapping of cement-based materials, Mater. Struct. 55 (2022) 131.
[45] M. Johnson, S. Baryshev, E. Thimsen, M. Manno, X. Zhang, I. Veryovkin, C. Leighton, E. Aydil, Alkali-metal-enhanced grain growth in Cu 2 ZnSnS 4 thin films, Energy Environ. Sci. 7 (2014) 1931–1938.
[46] N. Edanami, R.S.I. Belal, S. Takenaka, K. Yoshiba, R.E.B. Gutierrez, S. Takahara, N. Yoshiba, N. Ohkura, Y. Noiri, In vivo assessment of the calcium salt-forming ability of a new calcium silicate-based intracanal medicament: bio-C temp, Dentistry J. 11 (2023) 91.
[47] T.S. Duffy, C. Meade, Y. Fei, H.-K. Mao, R.J. Hemley, High-pressure phase transition in brucite, Mg (OH) 2, Am. Mineral. 80 (1995) 222–230.
[48] M.C. Hales, R.L. Frost, W.N. Martens, Thermo-Raman spectroscopy of synthetic nesquehonite—implication for the geosequestration of greenhouse gases, J. Raman Spectrosc. 39 (2008) 1141–1149.
[49] R.L. Frost, Raman spectroscopic study of the magnesium carbonate mineral hydromagnesite (Mg5 [(CO3) 4 (OH) 2]· 4H2O), J. Raman Spectrosc. 42 (2011) 1690–1694.
[50] P.J. Davies, B. Bubela, The transformation of nesquehonite into hydromagnesite, Chem. Geol. 12 (1973) 289–300.
[51] V. Mavromatis, C.R. Pearce, L.S. Shirokova, I.A. Bundeleva, O.S. Pokrovsky, P. Benezeth, E.H. Oelkers, Magnesium isotope fractionation during hydrous magnesium carbonate precipitation with and without cyanobacteria, Geochim. Cosmochim. Acta 76 (2012) 161–174.
[52] L. Hopkinson, K. Rutt, G. Cressey, The transformation of nesquehonite to hydromagnesite in the system CaO-MgO-H2O-CO2: an experimental spectroscopic study, J. Geol. 116 (2008) 387–400.
[53] G. Dercz, K. Prusik, L. Pajak, R. Pielaszek, J.J. Malinowski, W. Pudło, Structure studies on nanocrystalline powder of MgO xerogel prepared by the sol-gel method, Mater. Sci. 27 (2009).
[54] K.M. Saoud, S. Saeed, R.M. Al-Soubaihi, M.F. Bertino, Microwave assisted preparation of magnesium hydroxide nano-sheets, Am. J. Nanomater. 2 (2014) 21–25.
[55] L. Kumari, W. Li, C.H. Vannoy, R.M. Leblanc, D. Wang, Synthesis, characterization and optical properties of magnesium hydroxide micro-/nanostructures, APS March Meeting Abstracts (2009) 142.
[56] F.P. Glasser, G. Jauffret, J. Morrison, J.-L. Galvez-Martos, N. Patterson, M.S.-E. Imbabi, Sequestering CO2 by mineralization into useful nesquehonite-based products, Front. Energy Res. 4 (2016) 3.

[57] J. Epp, 4 - X-ray diffraction (XRD) techniques for materials characterization, in: G. Hübschen, I. Altpeter, R. Tschuncky, H.-G. Herrmann (Eds.), Materials Characterization Using Nondestructive Evaluation (NDE) Methods, Woodhead Publishing, 2016, pp. 81–124.
[58] M.E. Sanz-Montero, Ó. Cabestrero, M. Sánchez-Román, Microbial Mg-rich carbonates in an extreme alkaline lake (Las Eras, Central Spain), Front. Microbiol. 10 (2019) 148.
[59] Y. Wang, Z. Li, G.P. Demopoulos, Controlled precipitation of nesquehonite (MgCO3·3H2O) by the reaction of MgCl2 with (NH4)2CO3, J. Cryst. Growth 310 (2008) 1220–1227.
[60] P. Nie, T. Dong, S. Xiao, L. Lin, Y. He, F. Qu, Quantitative determination of thiabendazole in soil extracts by surface-enhanced raman spectroscopy, Molecules 23 (2018) 1949.
[61] J. Forsdyke, J. Lees, Carbonation Depth Measurement of Concretes Exposed to Different Curing and Preconditioning Conditions, Using Image-processing Tools, 2021.
[62] R.A. Robie, B.S. Hemingway, The enthalpies of formation of nesquehonite, MgCO3· 3H2O, and hydromagnesite, 5MgO· 4CO2· 5H2O, J. Res. U.S. Geol. Surv. 1 (1973) 543–547.
[63] L. Li, H. Yu, S. Zhou, V. Dao, M. Chen, L. Ji, E. Benhelal, Activation and utilization of tailings as CO2 mineralization feedstock and supplementary cementitious materials: a critical review, Mater. Today Sustain. 24 (2023) 100530.
[64] H. Nguyen, H. Santos, H. Sreenivasan, W. Kunther, V. Carvelli, M. Illikainen, P. Kinnunen, On the carbonation of brucite: effects of Mg-acetate on the precipitation of hydrated magnesium carbonates in aqueous environment, Cem. Concr. Res. 153 (2022) 106696.
[65] S. Ma, A.H. Akca, D. Esposito, S. Kawashima, Influence of aqueous carbonate species on hydration and carbonation of reactive MgO cement, J. CO2 Util. 41 (2020) 101260.
[66] J.F.W. Bowles, Hydroxides, in: D. Alderton, S.A. Elias (Eds.), Encyclopedia of Geology (Second Edition), Academic Press, Oxford, 2021, pp. 442–451.
[67] G. Giester, C. Lengauer, B. Rieck, The crystal structure of nesquehonite, MgCO3· 3H2O, from Lavrion, Greece, Mineral. Petrol. 70 (2000) 153–163.
[68] S. Lu, P. Yan, Y. Gao, C. Zhang, Theoretical investigation of the energies, structures, and growth properties of hydromagnesite surfaces, Cryst. Growth Des. 20 (2020) 3722–3731.
[69] R.R. Zigan F, The crystal structure comprises layers of edge-sharing Mg(O,OH)6 octahedra, Monatshefte 137 (1967) 137.
[70] M. Akao, S. Iwai, The hydrogen bonding of hydromagnesite, Acta Crystallogr. Section B Struct. Crystallogr. Crystal Chem. 33 (1977) 1273–1275.
[71] R. Hao, Investigation Into the Production of Carbonates and Oxides from Synthetic Brine Through Carbon Sequestration, Department of Engineering, University of Cambridge, 2017.
[72] A. Jarosinski, L. Madejska, MgCO3 obtaining from wastewaters generated during the acidic leaching of zinc concentrates, Minerlia Slovaca 42 (2010) 317–320.